Remote Sensing of Environment 277 (2022) 113060

Contents lists available at ScienceDirect

Remote Sensing of Environment

journal homepage: www.elsevier.com/locate/rse

Detecting crop phenology from vegetation index time-series data by improved shape model fitting in each phenological stage

Licong Liu [a,b], Ruyin Cao [a,*], Jin Chen [b], Miaogen Shen [b], Shuai Wang [b], Ji Zhou [a], Binbin He [a]

[a] School of Resources and Environment, University of Electronic Science and Technology of China, Chengdu, Sichuan 611731, China
[b] State Key Laboratory of Earth Surface Processes and Resource Ecology, Institute of Remote Sensing Science and Engineering, Faculty of Geographical Science, Beijing Normal University, Beijing 100875, China

ARTICLE INFO

Edited by Dr Marie Weiss

Keywords:
Crop phenology
Curve fitting
Shape model
Vegetation index time series
Crop classification

ABSTRACT

Crop phenology provides important information for crop growth management and yield estimations. The popular shape model fitting (SMF) method detects crop phenology from vegetation index (VI) time-series data, but it has two limitations. First, SMF assumes the same "relative position" of phenological stages for the pixels of the same crop type. This assumption is valid only if all target pixels, relative to the shape model, display a synchronized increase (or decrease) in length between any two phenological stages, which is uncommon in practice. Second, the variance in the resulting phenology estimates for a particular phenological stage is related to the stage itself; this makes it challenging to simulate spatial and temporal variations in crop phenology using SMF. Here, we address both limitations by developing the shape model fitting by the Separate phenological stage method ("SMF-S"). SMF-S uses a modified fitting function and an iterative procedure to match the shape model with the VI time series for each phenological stage in an adaptive local window. Comparisons between SMF-S and SMF in simulation experiments show the superior performance of SMF-S in different scenarios, regardless of noise. Comparisons involving winter wheat field observations from the North China Plain showed that the RMSE values averaged over nine phenological stages were smaller for SMF-S (RMSE = 9.5 d) than for SMF (RMSE = 13.4 d) and one variant of SMF (the shape model with accumulated growing degree days (SM-AGDD); RMSE=33.6 d). Moreover, SMF-S better described the spatial variations (i.e., variance) in the results and captured the temporal shifts in multiple phenological stages. In the derived regional phenology maps of winter wheat on the North China Plain, SMF-S generated more reasonable spatial patterns, whereas SMF underestimated (overestimated) the variance in the early (late) phenological stages. We expect that the improved crop phenology estimates obtained with SMF-S could benefit various agricultural activities.

1. Introduction

The phenological stages of crops, as a calendar of seasonal crop growth dynamics, provide important information for agricultural activities such as fertilizer management, irrigation scheduling, disease prevention, and crop type classification (Gao and Zhang, 2021; Sakamoto et al., 2010; Zhong et al., 2016). Understanding crop phenology is also essential for obtaining crop yield estimates (Bolton and Friedl, 2013; Brown et al., 2012); for example, the occurrence of environmental stress in some phenological stages may greatly reduce the crop yield (Wang et al., 2020). Currently, regional-scale crop phenology information can be obtained from satellite-based remotely sensed data. A few methods have been proposed to estimate this information from time series of synthetic aperture radar data or optical vegetation indices (VIs) (Bhogapurapu et al., 2021; Gao et al., 2020; Schlund and Erasmi, 2020; Yang et al., 2021; Zhang et al., 2020).

Threshold-based and function-fitting methods are two traditional approaches used to detect vegetation phenology. In threshold-based methods, phenology is determined to be the date when the VI reaches a fixed value (absolute threshold) or a given amplitude of the seasonal changes in VI values (relative threshold) (see review by Zeng et al., 2020). For example, Boschetti et al. (2009) estimated the key phenology information for rice in Italy from the normalized difference vegetation index (NDVI) time series data provided by the MODerate-resolution Imaging Spectroradiometer (MODIS). The start of the season (emergence) was defined as the date when the NDVI first increased to 10% of

* Corresponding author.
E-mail address: cao.ruyin@uestc.edu.cn (R. Cao).

https://doi.org/10.1016/j.rse.2022.113060
Received 8 September 2021; Received in revised form 29 March 2022; Accepted 27 April 2022
Available online 10 May 2022

the difference between the left-minimum NDVI value and the maximum NDVI value, and the growth peak (heading) was defined as the date corresponding to the midpoint between the right 90% and left 90% values of the NDVI curve. Function-fitting methods have been designed to simulate VI time-series data using mathematical functions such as logistic functions, the Savitzky–Golay filter, and wavelet filters (Beck et al., 2006; Cao et al., 2018b; Sakamoto et al., 2005; Wardlow et al., 2006; Zhang et al., 2003). Phenological events are identified as the dates when the fitted curve exhibits specific mathematical features. Zhang et al. (2003) used a piecewise logistic function to fit MODIS VI time-series data and determined four phenological events (i.e., green-up, maturity, senescence, and dormancy) to be the timing of four inflection points (i.e., changes in the rate of curvature) in the fitted curve. Their logistic method was used to generate the MODIS phenology product MCD12Q2 v5, which was also used for estimating crop phenology (Bolton and Friedl, 2013). In addition, Manfron et al. (2017) defined the timing of the peak and minimum values in smoothed VI time-series data of winter wheat as the heading and sowing dates. Sakamoto et al. (2005) used the timing of feature points in smoothed VI time series (e.g., the minimum, maximum, and inflection points) as the phenological stages of rice. Yang et al. (2020) determined the phenological stages of various crops from feature points (e.g., the peaks of the first and second derivations of the VI time series). Diao (2019) innovatively used a complex network to resolve the transition dates of spectral reflectance time series to obtain the maturity stage of maize and the leaf-drop stage of soybean. In fact, the feature points estimated from fitted VI time series normally indicate the transition dates of vegetation greenness changes, which are somewhat different from the crop phenology definitions used in agriculture; thus, these feature points may be difficult to associate with the agronomic stages of various crops (Guo et al., 2016; Sakamoto, 2018). For example, the flowering date of soybean, a key phenological stage related to yield, may be difficult to detect from feature points due to the lack of distinctive features in VI time-series data (Zeng et al., 2016). Such challenges also exist with regard to the phenological stages of other crop types, such as the jointing stage of winter wheat.

To estimate crop phenology, Sakamoto et al. (2010) proposed a novel method based on the concept of shape model fitting (SMF), which has shown considerable potential for detecting phenological information in multiple crops (Sakamoto, 2018; Sakamoto et al., 2010; Zeng et al., 2016, 2020; Zhang et al., 2020; Zhou et al., 2020). The SMF method uses a shape model (referred to as $g(x)$), which can be a VI time series with corresponding ground phenology observations, to match the seasonal VI time series of the same crop type (referred to as $h(x)$) based on linear shift and scaling steps, expressed as:

$$\widehat{g}(\mathrm{x}) = \mathrm{yscale} \times [g(xscale \times (x + tshift)) + bias] - bias \tag{1}$$

where *bias* is a fixed value for each crop type and is determined by the background VI value, *xscale* and *yscale* are the scaling factors in the two dimensions (i.e., time and the VI value), and *tshift* is the time shift factor. These three factors are determined by minimizing the root mean square error (RMSE) between $h(x)$ and $\widehat{g}(\mathrm{x})$. In SMF, it is assumed that the phenological stages in the target VI curve have the same "relative position" as those in the reference VI curve; thus, all phenological stages in $h(x)$ (expressed as p^i_{est}, $i = 1, \ldots n$)can be estimated from the corresponding stages in $g(x)$ (expressed as p^i_0, $i = 1, \ldots n$) using *xscale* and *tshift* as follows:

$$p^i_{est} = \frac{1}{xscale} \times p^i_0 - tshift, i = 1, \ldots n \tag{2}$$

Eq. 2 has corrected errors in SMF-derived phenology estimation equations in previous studies (see Appendix A for the corrigendum). SMF does not focus on mathematical feature points but uses a geometrical pattern to associate VI time series with the specific agronomic stages observed in the field. The shape model concept has two obvious strengths. First, the model combines ground agronomic observations with specific positions in the curves of VI time series data; thus, any prior phenological information available for a particular crop type can be easily incorporated into the shape model (Sakamoto et al., 2010). Second, the model avoids the use of predefined mathematical functions to simulate the annual crop growth trajectory, as VI time series may deviate from a predefined function due to the regulation of vegetation growth by various factors (Cao et al., 2015). The SMF method has been shown to be more accurate than methods that utilize predefined mathematical features to obtain maize and soybean phenology estimations, with smaller RMSE values, ranging from 2.9 to 7.0 d (Sakamoto et al., 2010). Subsequent studies have continued to improve the shape model used in the SMF method. These studies mainly challenged the assumption in SMF that the shape model can be linearly scaled to match the VI time-series data of the target pixels due to the large variations in crop growth patterns among sites and years. To reduce such variations, Zeng et al. (2016) incorporated a crop growth model into the SMF method by employing the accumulated temperature and photoperiod (i.e., the accumulated photothermal time (APTT)) to simulate the crop growth progress. Thus, the calendar time on the x-axis of the VI time series is replaced by the APTT. The SMF-APTT method was shown to reduce errors when analyzing maize and soybean phenology in eastern Nebraska, USA. Under the same methodological framework, Zhou et al. (2020) proposed using accumulated growing degree days (AGDDs) to simulate the crop growth progress. The SM-AGDD method was shown to achieve an improved accuracy when estimating wheat phenology at one local site in China. Sakamoto (2018) expanded the SMF method by using a new procedure to calibrate shape models corresponding to 36 crop development stages of eight crop types in the USA. This calibration procedure requires a crop phenology report for each US state but does not require ground phenology observations at individual sites, thus simplifying the associated data requirements. Recently, the shape model concept was further extended for use in spatiotemporal data fusion applications (Sun et al., 2021; Zhang et al., 2020). For example, Sun et al. (2021) defined a shape model for a particular crop type using MODIS time-series data and used this model to fit cloud-free Landsat or Harmonized Landsat and Sentinel-2 observations to generate 30-m NDVI time-series data.

Although the SMF method offers promise for obtaining crop phenology estimations, it does have two inherent limitations that need to be addressed. First, SMF uses a shape model to match the entire growing season of the target VI time series through linear shifts and scaling. This global matching strategy could lead to synchronized changes in the lengths between two phenological stages, which can be formulated as:

$$p^i_{est} - p^j_{est} = \frac{1}{xscale} \times \left(p^i_0 - p^j_0\right)\ i \neq j \in \{1, \ldots n\} \tag{3}$$

In other words, relative to the shape model, target pixels can undergo synchronized increases (or decreases) in length between any two phenological stages. This condition is difficult to satisfy, particularly for crop types with long growing seasons (Zeng et al., 2016). If synchronized changes are assumed, it is impossible to investigate the relationships among multiple phenological stages. For example, there is a proportional relationship between the early phenological period (e.g., $p^i_{est} - p^{i-1}_{est}$) and the late phenological period (e.g., $p^{i+1}_{est} - p^i_{est}$) for all target pixels (i.e., $(p^i_{est} - p^{i-1}_{est})/(p^{i+1}_{est} - p^i_{est}) = (p^i_0 - p^{i-1}_0)/(p^{i+1}_0 - p^i_0)$). Second, the scaling factor in the SMF function is related to the phenological stages (see Eq. 2), and this leads to the dependence of the variance in the phenology estimates for a particular phenological stage on the stage itself (see section 2 for the corresponding derivations). Since the shape model is stretched from the left endpoint, phenology estimates by SMF usually have larger variance in the later stages than in the earlier stages in practice. The underestimation of the variance in the earlier stages may further lead to small temporal trends in these stages. The spatial patterns and temporal changes in phenology are two primary foci

in phenological research, but they may be misinterpreted when SMF-derived phenology estimates are used.

Therefore, we developed a new crop phenology detection method, called SMF by separate phenological stages (SMF-S). The SMF-S method modifies the fitting function to correct for the dependence of the phenological variance on the phenological stage. To address the unsynchronized phenological changes throughout the entire growing season, SMF-S uses an iterative procedure to match the shape model with the target VI curve in each phenological stage in an adaptive local window. We tested the performance of SMF-S using simulation experiments, field phenology observations, and regional satellite data.

2. SMF-S method

The SMF-S method was developed from the SMF framework to address the aforementioned limitations in the SMF process. SMF-S performs shape model fitting in each phenological stage by using a modified fitting function and adaptive local windows (Fig. 1). The key improvements made in the SMF-S method are detailed below.

2.1. Using the modified fitting function for each phenological stage

In SMF, all phenological stages in the target curve $h(x)$ (p^i_{est}, $i = 1, \ldots n$) can be estimated from the corresponding stages in the shape model $g(x)$ (p^i_0, $i = 1, \ldots n$) according to Eq. 2. Thus, the variance in p^i_{est} can be expressed as follows:

$$D\left(p^i_{est}\right) = D\left(\frac{1}{xscale} \times p^i_0 - tshift\right) \tag{4}$$

where $D(\cdot)$ indicates the variance function. Eq. 4 represents the variance in the sum of "$\frac{1}{xscale} \times p^i_0$" and "$-tshift$". By using an expansion function for the sum of the variance (i.e., $D(X+Y) = D(X) + 2COV(X,Y) + D(Y)$),

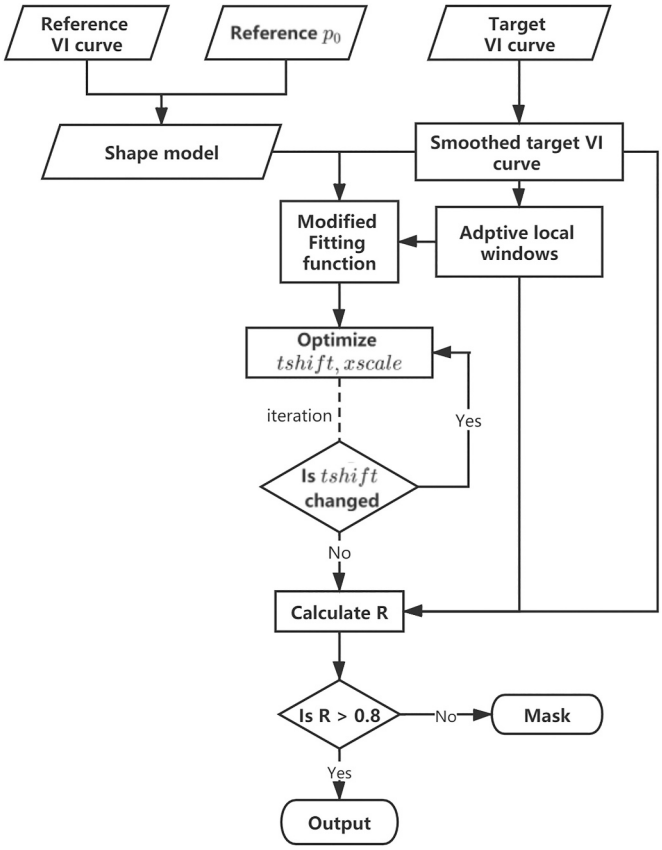

Fig. 1. Flowchart of the SMF-S method.

Eq. 4 can be reformulated as follows:

$$D\left(p^i_{est}\right) = D\left(p^i_0 \frac{1}{xscale}\right) + 2COV\left(p^i_0 \frac{1}{xscale}, -tshift\right) + D(-tshift)$$

$$= \left(p^i_0\right)^2 D\left(\frac{1}{xscale}\right) + 2p^i_0 COV\left(\frac{1}{xscale}, -tshift\right) + D(-tshift) \tag{5}$$

where $COV(\cdot)$ indicates the covariance function. Since *xscale* and *tshift* are acquired by nonlinear optimization, it is difficult to further simplify this equation. However, it is clear that $D(p^i_{est})$ is related to p^i_0 with an upward quadratic function. In practice, by using simulated data and regional satellite-derived data, we observed an increase in $D(p^i_{est})$ with p^i_0, that is inconsistent with the real trends in field phenology observations (see section 4). To correct for the dependence of $D(p^i_{est})$ on p^i_0, in the SMF-S method, a shape model is fit for each phenological stage. The SMF fitting function is modified as follows:

$$\hat{g}\left(x, p^i_0\right) = g\left(xscale_i \times x + (1 - xscale_i) \times p^i_0 + xscale_i \times tshift_i\right), i = 1, \ldots n \tag{6}$$

There are two main differences between the SMF-S and SMF fitting functions (cf. Eq. 6 and Eq. 1). First, the SMF-S function removes the *yscale* and *bias* parameters because phenology estimates are controlled by the time dimension, whereas these two parameters account for the VI value differences between $g(x)$ and $\hat{g}(x)$ (i.e., the VI value dimension). Reducing the number of parameters can strengthen the nonlinear parameter optimization process and improve the computational efficiency (see discussion section 5.2). Second, to match a particular phenology stage p^i_0, it may be optimal to perform the stretch and shift around the position of p^i_0. However, the applied change in *xscale* in the SMF fitting function (i.e., $xscale_i \times x$ in Eq. 1) induces stretching from the left endpoint (Fig. 2). To induce stretching at both sides around the position of p^i_0, we introduce the term $(1 - xscale_i)$?—p^i_0 into the SMF-S fitting function, which compensates for the time shift caused by stretching (Fig. 2). For phenological stage p^i_0 in $g(x)$, SMF-S estimates the corresponding phenological stages in $\hat{g}(x)$ as:

$$xscale_i \times p^i_{est} + (1 - xscale_i) \times p^i_0 + xscale_i \times tshift_i = p^i_0,\ i = 1, \ldots n$$

$$p^i_{est} = p^i_0 - tshift_i, i = 1, \ldots n \tag{7}$$

Eq. 7 suggests that SMF-S stretches in the local segment of the VI time series centered at p^i_0 (Fig. 2).

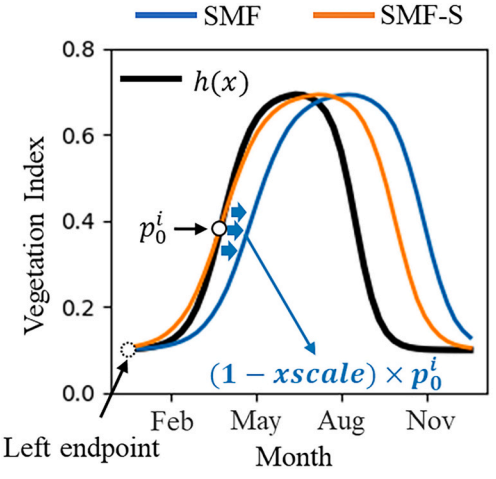

Fig. 2. Influence of stretch operations on the shape model functions of SMF (blue) and SMF-S (orange). In the SMF method, stretching is performed from the left endpoint, leading to a time shift of $(1 - xscale_i) \times p^i_0$ in phenological stage p^i_0.

2.2. Determining adaptive local windows

The SMF-S function provides the opportunity to more accurately match the local segment of the VI time series centered at p_0^i. In this process, the two parameters in Eq. 6 are estimated by maximizing the correlation coefficient between $\widehat{g}\left(x, p_0^i\right)$ and $h(x)$ in a local VI time-series segment as follows:

$$tshift_i, xscale_i = \underset{tshift_i, xscale_i}{\operatorname{argmax}} R\left(\widehat{g}\left(x, p_0^i\right), h(x)\right), \quad i = 1, \ldots n$$

$$x \in \left(p_0^i - tshift_i - w, p_0^i - tshift_i + w\right) \tag{8}$$

where w is the half-window width of the local segment of the VI time series. Logically, w should be determined by considering both the local curve features in a particular phenological stage and the data noise levels. Therefore, SMF-S determines an adaptive window by using the look-up table strategy. Taking the application of SMF-S in a region as an example, we generate the look-up table in three steps.

In the first step, we use the Savitzky–Golay (SG) filter to smooth all the VI time-series data and further generate a number of smoothed VI time-series sample curves for a given crop type by aggregating the VI time series of the same crop type within each 3 × 3 spatial window. Pixels exhibiting extremely large differences between the original and filtered VI time series (> 3 times the standard deviation of the difference) are excluded from the generation; these pixels account for less than 0.5% of all pixels. We randomly select 100 sample curves. Based on a reference shape model, SMF-S is employed to detect the phenological information corresponding to these sample curves with a relatively small w value of 30 d. Using a small window is reasonable because the generated sample curves are fairly smooth and have shapes similar to that of the shape model. The estimates are regarded as the true phenological states of the sample curves.

In the second step, we simulate random negative noise in the sample curves as follows:

$$VI_{j\_noise} = VI_j - \left|N(\mu = 0, \sigma)_j\right| \times VI_j, j = 1, \ldots 46 \tag{9}$$

where j indicates the jth VI value in the time series. Normally distributed random noise is generated with a mean value of zero and a standard deviation of σ. We consider different noise levels by varying σ from 5% to 40% in increments of 5% (for a total of eight noise levels). At each noise level, we conduct 100 simulations for each sample curve; thus, a total of 10000 simulations (100 simulations × 100 sample curves) are performed.

In the third step, we estimate the phenological information on the SG-filtered sample curves by varying w from 30 to 180 d in increments of 15 d. The optimal w value at each noise level for a given phenological stage is determined as the value that yields the smallest difference between the estimate and the reference phenology for the sample curves. Therefore, one lookup table (with noise level columns and optimal w rows) can be generated for each phenological stage. In practical applications, however, the noise levels of target pixels are unknown. Therefore, we used a noise level surrogate represented as the RMSE value derived from the local VI time series between the noise-simulated and SG-filtered sample curves. Here, the local range of the ith phenological stage is determined as $[p_0^i - 45, p_0^i + 45]$. Normally, VI time series with high noise levels have large RMSE values between the original and SG-filtered VI time series. The w value at any noise level, as indicated by the RMSE, can be determined by linearly interpolating the look-up table.

SMF-S uses an iterative program to determine $tshift_i$ and $xscale_i$ in the shape model fitting. Specifically, with an initial $xscale_i$ value of 1.0, we first change $tshift_i$ from −45 to 45 d at a step of 1 d and determine the optimal $tshift_i$ value as that when the objection function is maximized (with Eq. 8). Next, we fix the initially determined $tshift_i$ value and estimate an optimal $xscale_i$ value in a similar way by changing the $xscale_i$ value from 0.8 to 1.2 in increments of 0.01. This process is repeated, and the iteration is terminated when $tshift_i$ no longer changes. In practice, SMF-S provides stable $tshift_i$ values within four iterations for more than 99% of pixels when mapping winter wheat phenology on the North China Plain. In some cases, the shape model and target VI time series may not be so similar owing to extremely high noise or incorrect crop type identification. We remove the corresponding final phenology estimates if their correlation coefficients (based on Eq. 8) are <0.8 (Fig. 1). The removed pixels account for less than 1.0% of all winter wheat pixels in the North China Plain area.

3. Data and experiments

The performance of SMF-S was assessed by conducting simulation experiments and deriving winter wheat phenology estimates. We compared the SMF-S method with the SMF and SM-AGDD methods (Zhou et al., 2020). Because SM-AGDD requires temperature data as an input, this method was excluded from the simulation experiments.

3.1. Assessments using simulation experiments

First, we conducted simulation experiments to test the performance of SMF-S. Specifically, we followed the method outlined by Zhang et al. (2003) to simulate annual VI time-series data by using two piecewise logistic functions (i.e., the rising phase from the green-up stage to the time of peak VI and the descending phase from the peak VI timing to the dormancy stage). Each phase was simulated by the following four-parameter logistic function:

$$VI(t) = \frac{c}{e^{b(t-t_0)}} + d \tag{10}$$

where the parameters c and d represent the amplitude and the background VI value, respectively; t_0 represents the date when $VI(t)$ reaches 50% of its amplitude; and b describes the rate of change of $VI(t)$ at t_0. In the simulations, we generated 10000 annual VI time series by randomly determining the four parameters within the given ranges. The values of c and d were within [0.5, 0.7] and [0, 0.2], respectively. The values of t_0 and b were randomly determined within [80, 120] and [−0.08, −0.05] for the rising phase and within [240, 280] and [0.05, 0.08] for the descending phase. The four key phenological stages were defined based on the simulated VI time series data according to the following formulations proposed by Shang et al. (2017):

$$greenup = t_0 + \frac{ln\left(5 + 2\sqrt{6}\right)}{b_{rising}}$$

$$maturity = t_0 - \frac{ln\left(5 + 2\sqrt{6}\right)}{b_{rising}}$$

$$senescence = t_0 - \frac{ln\left(5 + 2\sqrt{6}\right)}{b_{descending}}$$

$$dormancy = t_0 + \frac{ln\left(5 + 2\sqrt{6}\right)}{b_{descending}} \tag{11}$$

where b_{rising} and $b_{descending}$ indicate b for the rising and descending phases. We compared SMF-S with SMF in both a no-noise scenario and a scenario with different noise levels. Random negative noise ranging from 0% to 30% was added to the simulated annual VI time-series data. To ensure a fair comparison, both the SMF-S and SMF methods used the same shape model (Fig. 3), in which each parameter value in the logistic function was determined to be the median value of the corresponding simulation range.

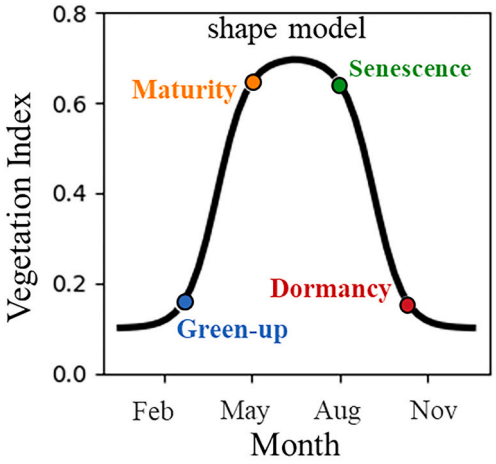

Fig. 3. Reference curves with corresponding reference phenology (i.e., the shape model) used in the simulation experiment.

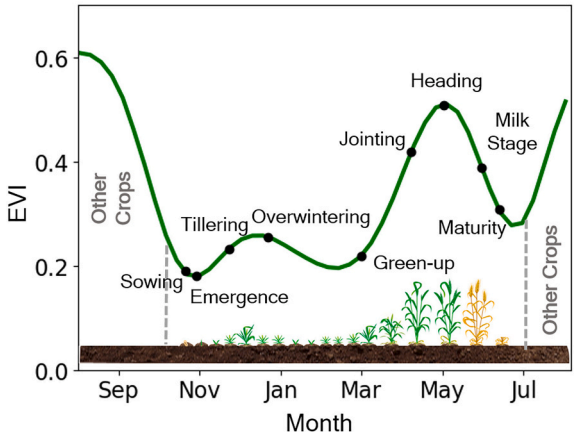

Fig. 5. EVI time series of winter wheat with the corresponding phenological stages.

3.2. Assessments for estimating winter wheat phenology

3.2.1. Winter wheat on the North China Plain

We tested the SMF-S method in the detection of winter wheat phenology on the North China Plain (29°–42°N, 105°–122°E; Fig. 4). Winter wheat there accounts for 60% of wheat production in China (Dong et al., 2020). Other crops include summer maize, soybean, and rice, which are rotated with winter wheat (Cao et al., 2018a). In this area, winter wheat is sown mainly after September and is harvested before the following July, in a relatively complex annual VI time series with two growth stages (Fig. 5). Nine winter wheat phenological stages can be defined according to the field phenological records provided by the National Meteorological Information Center, China Meteorological Administration (Table 1). Fig. 5 shows the annual VI time-series data for winter wheat with the nine corresponding phenological stages. The emergence stage, which is defined as the occurrence of the first green leaflet from the coleoptile, is near the point corresponding to the minimum EVI value in the annual VI time-series data. The tillering and overwintering stages occur on the two sides of the first local maximum EVI value. The green-up stage describes the date on which the leaf sheaths begin to lengthen, which approximately corresponds to the point when the EVI value starts to increase in spring. When the tip of the ear is exposed from the sheath of the flag leaf, winter wheat is considered to have reached the heading stage; this stage occurs in conjunction with the maximum EVI value. The maturity stage is defined as the time at which green plant tissues brown; this stage occurs near the local minimum EVI value after June. For comprehensive information about

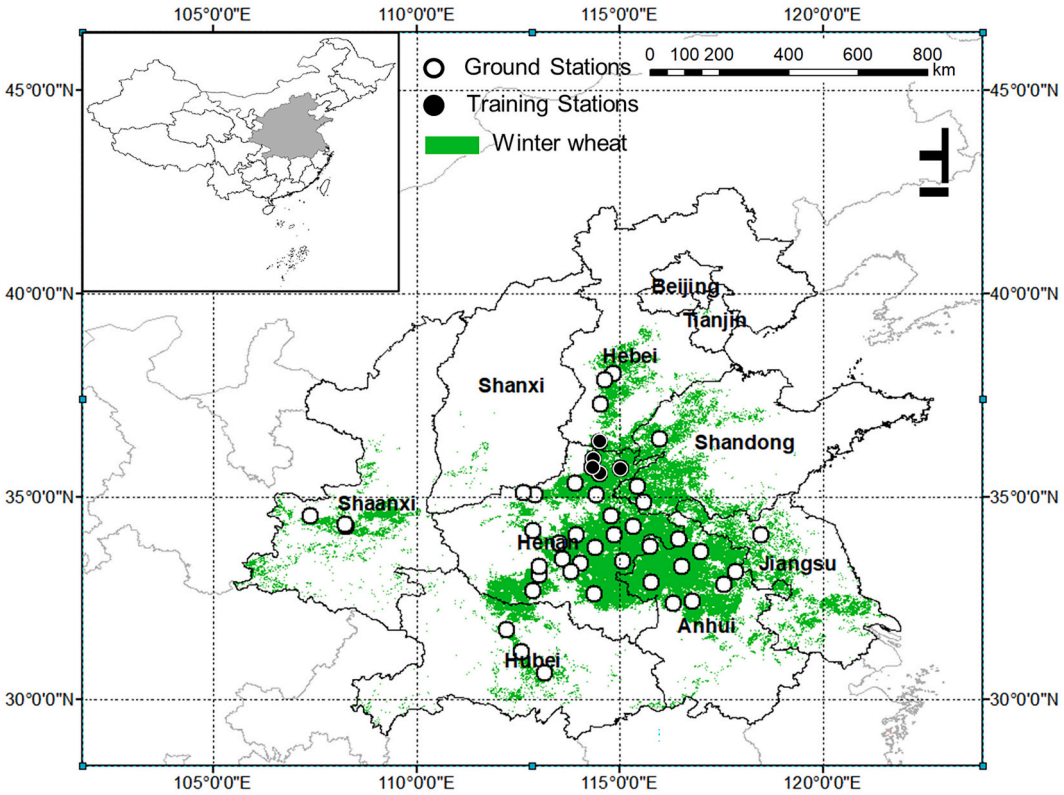

Fig. 4. Spatial distribution of winter wheat on the North China Plain (shown in insert). Data from the training stations were used to generate the shape model for winter wheat.

Table 1
The nine phenological stages of winter wheat.

Phenological stages	Description
Sowing	Seeds are sown
Emergence	The first green leaflet emerges from the coleoptile, approximately 2.0 cm long
Tillering	The tip of the first tiller exposed in the leaf sheath is approximately 0.5 to 1.0 cm
Start of overwintering period	Plants with adequate tillers are needed before winter dormancy to ensure the maximum yield potential
Spring green-up	Winter wheat resumes growth, and the heart leaves grow 1.0–2.0 cm.
Jointing date	First node of the stem becomes visible as a result of internode elongation
Heading date	The tip of the ear is exposed from the sheath of the flag leaf
Milky ripe	The kernels in the middle of the ear (naked oats, oat tops) reach normal size and are yellow–green
Maturity date	More than 80% of the grains turn yellow, the glumes and stems turn yellow, and only the first and second nodes in the upper part are still slightly green

all nine phenological stages, please refer to Table 1.

We calculated enhanced vegetation index (EVI) time-series data during the 2008–2016 period from the MOD09A1 reflectance product (https://lpdaac.usgs.gov/tools/). The data had an 8-d temporal resolution and a 500-m spatial resolution. We first replaced cloud-contaminated values in the EVI time-series data by a linear interpolation process and then smoothed the time-series with the SG filter (Chen et al., 2004). Winter wheat classification maps representing the 2008–2016 period were generated from the EVI time-series data using the method described by Qiu et al. (2017).

3.2.2. *Assessments with the winter wheat phenology observations collected at ground stations*

We compared the phenological estimates derived using SMF-S, SMF, and SM-AGDD with field phenology observations. The number of observation stations varied between 90 and 130 from 2008 to 2016. To reduce uncertainty, we adopted the following criteria to screen unsuitable stations and crop phenology observations. First, to ensure a relatively stable distribution of winter wheat in our analyses, we preserved only those pixels that were identified as winter wheat in all 9 years (Fig. 4). Second, we removed those stations at which the winter wheat pixel percentages were <20% of the total pixels within the 20 km × 20 km expanse centered at the station location. The numbers of remaining ground stations for each stage in each year are summarized in Table 2. Because the specific field phenology observation dimensions at each station are not provided, we averaged the winter wheat EVI time-series data within an area of 20 km × 20 km by assuming little variation in the climate conditions in each small area. The winter wheat phenological information was estimated from the averaged EVI time series by using different methods, and the resulting estimates were compared with the corresponding field phenology observations. We recognize that uncertainty may still exist due to the different spatial scales between the field observations and satellite data. To address this difference, we estimated the winter wheat phenological stage from the averaged EVI time series data in smaller areas (e.g., 10 km × 10 km and 5 km × 5 km). The phenology estimates obtained at different spatial scales for SMF and SMF-S exhibited small differences (< 2 d) without outliers (Fig. S1). The slightly larger differences between different spatial scales for SM-AGDD are caused by the extremely large phenology estimation errors for this method (see section 4.2 for explanations). The results of this investigation suggest that the field observation comparisons are less affected by spatial scales within the range of 5–20 km. We further quantified the spatial phenological heterogeneity by calculating the standard deviation (SD) of the phenology estimates for winter wheat pixels within a 20 km × 20 km area around each station. The results showed that the SD values averaged over all stations are much smaller than the RMSE values of the phenological estimates (Fig. S2). Thus, comparisons between remotely-sensed phenology and field observations are expected to be acceptable at these ground stations.

Next, we determined the shape models (i.e., reference curves with reference phenology) for SMF-S, SMF, and SM-AGDD (Fig. 6). For SMF-S and SMF, the reference curve was generated by averaging the multiyear EVI time-series data at the central five training stations (denoted as ● in Fig. 4). The reference phenology was defined as the mean of the corresponding phenology observations at the five stations (refer to Sakamoto et al., 2010). Following the method of Zhou et al. (2020), the SM-AGDD reference curve was generated as follows. We first fit the AGDD-VI time-series curves using the double logistic function. Then, each fitted curve was normalized using the maximum and minimum values on the curve. Finally, the SM-AGDD reference curve was determined by averaging the curves over the five central stations. In the SM-AGDD method, a fixed base temperature of 3 °C was used for accumulating temperature. On the North China Plain, however, the average temperature is normally lower than 3 °C before spring. These early phenological stages are thus relatively concentrated in the shape model of SM-AGDD (Fig. 6b). According to Sakamoto et al. (2010), the VI values of the reference curve outside the growth period should be replaced by fixed values. On the North China Plain, there are normally two crop cycles within a year. Due to this multiple cropping scheme, the minimum VI values (i.e., the background VI values) differ between the two sides of the maximum VI value on the annual curve (i.e., from August 1 in the previous year to the current year). We thus used two different fixed values for the two sides of the reference curve (see the dashed line in Fig. 6). The *bias* parameter in SMF (Eq. 1) was determined to be the mean value of the two fixed values. We noticed that Sakamoto (2018) determined an identical fixed VI value (i.e., the *bias* parameter used in SMF) as the minimum VI value at the point backward from the maximum point. We also tested an identical fixed VI value but found that the RMSE values of the phenology estimates obtained with SMF decreased substantially (cf. Fig. S3a and Fig. 9a); this may have been due to the alterations made to the phenological characteristics in the shape model. In subsequent applications, the VI time-series curves of the target pixels were preprocessed using a similar procedure as that used for the shape model.

Table 2
Number of stations that recorded available winter wheat phenological stage information each year.

Phenological stages	2008	2009	2010	2011	2012	2013	2014	2015	2016	Total
Sowing	19	19	18	21	19	31	34	35	33	229
Emergence	19	19	20	18	20	33	34	35	34	232
Tillering	19	19	21	20	18	31	32	36	31	216
Spring green-up	10	13	14	15	13	17	27	22	29	160
Overwintering	12	12	13	12	12	21	23	28	26	159
Jointing date	16	18	19	20	17	34	34	35	38	231
Heading date	18	19	20	20	20	33	34	33	38	235
Milky ripe	19	21	21	18	21	32	34	33	37	236
Maturity date	19	20	21	19	20	33	34	32	36	234

Note: Not all nine phenological stages were recorded at each station.

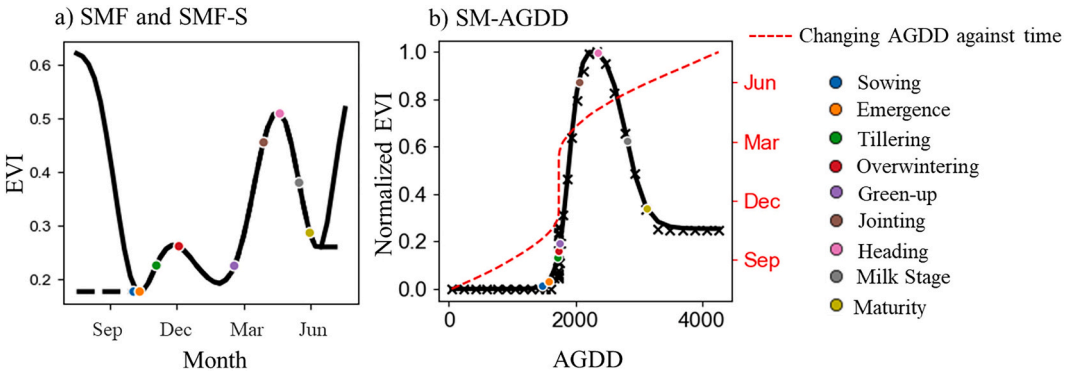

Fig. 6. Reference curves with corresponding reference phenology (color points) for different methods for winter wheat phenology estimations on the North China Plain: (a) SMF-S and SMF; (b) SM-AGDD. The black dashed line in panel (a) indicates the replacement of the VI values outside of the winter wheat growing season. The red dashed line in panel (b) represents the changes in the AGDD over time (see the right Y axis).

3.2.3. Assessment of winter wheat phenology mapping on the North China Plain

We further compared the SMF-S and SMF methods with regard to the ability of these methods to map regional winter wheat phenology. The SM-AGDD method was excluded from this regional mapping process because it exhibited substantially large errors when the results were compared with the field phenological observations (see Fig. 9 and the corresponding explanation of performance in the Discussion section 5.1). The SMF-S and SMF methods used the same shape model (as shown in Fig. 6A). We investigated the differences in the regional phenology maps derived with SMF-S and SMF.

4. Results

4.1. Comparisons in simulation experiments

We first conducted quantitative assessments using simulation experiments in the no-noise scenario (Fig. 7a-b). SMF-S performed better than SMF, obtaining smaller RMSE values and higher correlations between the phenology estimates and the true values; for example, when estimating the green-up date, the RMSE derived by SMF-S was 0.69 d, while that obtained by SMF was 4.42 d. These results suggest that SMF-S can better capture phenological metrics on EVI time-series data than SMF can. The analytic expression (Eq. 5) reveals the inherent limitation of SMF; the variance in the phenology estimates is related to the phenological stages themselves. Here, we calculated the standard deviation (SD) of phenology estimates derived using SMF and found that the SD increased with the phenological stage and was underestimated for early stages (e.g., the green-up date; Fig. 7c). In contrast, the SD of phenology estimates derived using SMF-S is more consistent with the true SD.

We next investigated the effect of noise in the EVI time series on the resulting phenology estimates (Fig. 8). We show only the changes in the green-up date and maturity date estimates considering the noise levels because of the similarity of the results between the green-up date and the dormancy date and between the maturity date and the senescence date. SMF-S performed better than SMF at all noise levels, although the accuracy of both methods decreased as the noise level increased. The better performance of SMF-S, particularly at high noise levels, can be partially attributed to its use of adaptive local windows. To confirm this explanation, we tested SMF-S using randomly determined w values (half-width of the window) ranging from 30 to 180 d and calculated the mean phenology estimates (referred to as the "Mean SMF-S" results; see the black dashed lines in Fig. 8a, b, d, e). Without using the adaptive local windows, the phenology estimation errors of SMF-S indeed increased and became even larger than those of SMF with regard to the maturity date at 20% noise (Fig. 8d). We examined the average w values used in SMF-S at different data noise levels and found that w increased with noise levels for the maturity date but varied little for the green-up date (Fig. 8c, f). At the green-up date, the EVI values are small; thus, the relative negative noise added in the time series does not dramatically decrease the time series values. When w increases, however, the increase in VI noise outside the local range of the green-up date may greatly affect the performance of shape model fitting. This VI noise trade-off inside and outside the local range of the green-up date may account for the small variations in w observed at this stage.

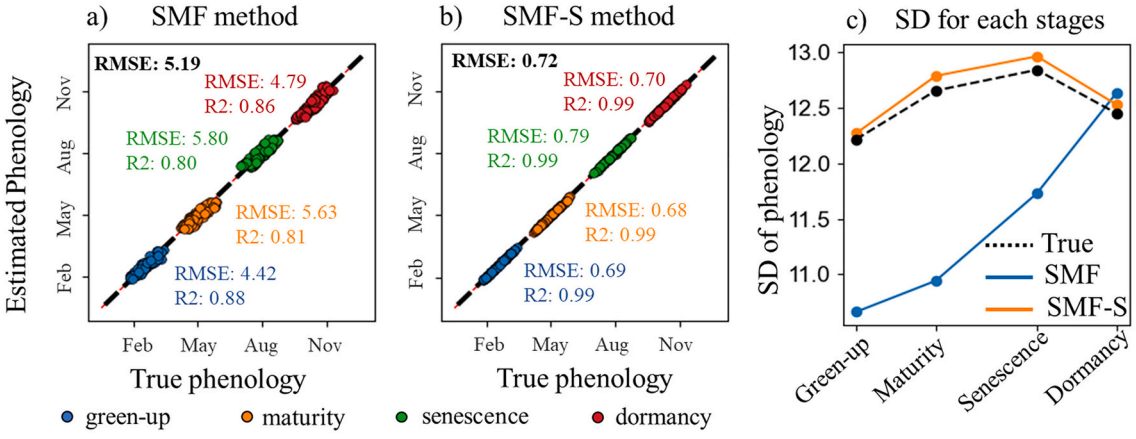

Fig. 7. Performance of the (a) SMF and (b) SMF-S methods in the no-noise scenario. (c) SD of phenology estimates derived using the SMF and SMF-S methods for four phenological stages.

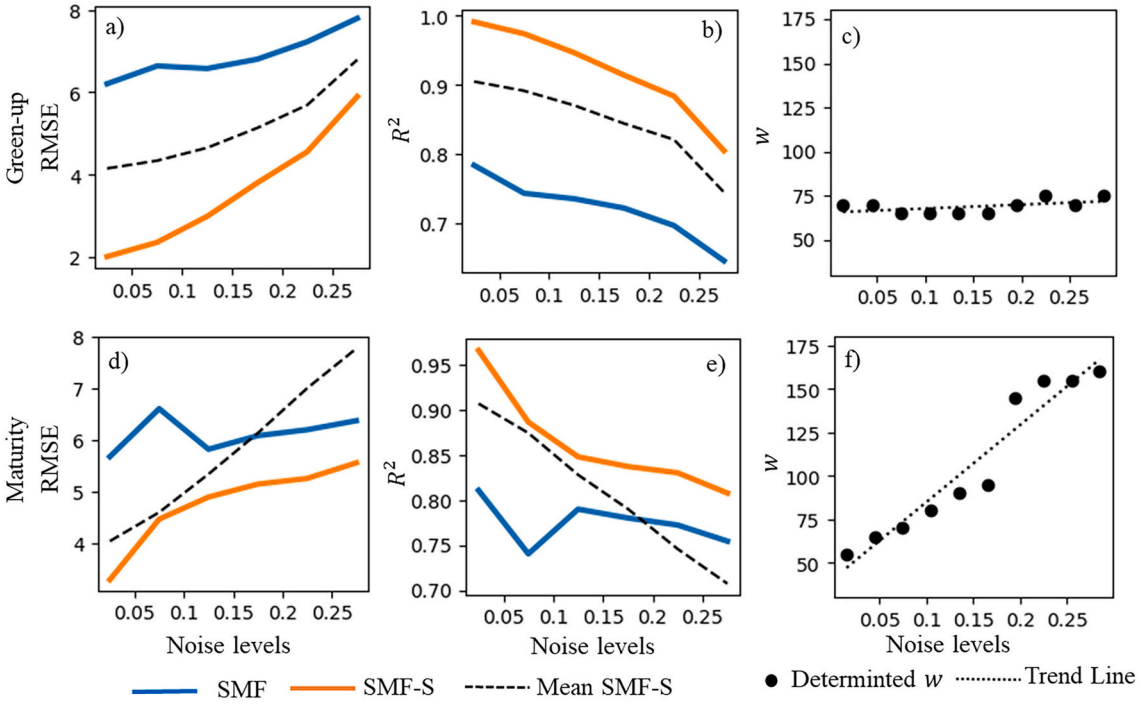

Fig. 8. (a, d) RMSE, (b, e) R^2, and (c, f) determined *w* of (a–c) the green-up date (GUD) and (e–f) maturity date (MD) with increasing noise levels in the two methods.

4.2. Comparisons of winter wheat phenological estimates at ground stations

We quantitatively compared the SMF-S method to the SMF and SM-AGDD methods regarding the ability of these methods to estimate winter wheat phenology at ground-based phenological observation stations. To implement the SM-AGDD method, we used the corresponding air temperature data recorded at the associated meteorological stations. In general, SMF-S achieved smaller phenology estimation errors than the other two methods. The RMSE values of SMF-S, SMF, and SM-AGDD averaged over the nine phenological stages were 9.5, 13.4, and 33.6 d, respectively (Figs. 9a-c; each panel also includes the RMSE value corresponding to each phenological stage). The worst SM-AGDD performance was mainly due to the obviously larger estimation errors obtained for the first five phenological stages, which is discussed in depth in section 5.1. Thus, we did not include SM-AGDD in further analyses or subsequent experiments due to its large estimation errors. Regarding the SMF method, there was little variation in the phenology estimates derived by SMF for the early phenological stages (bottom left of Fig. 9a). SMF-derived estimates seem to be negatively correlated with field-observed phenology at these early stages (e.g., tillering and overwintering). Explanations for this unusual pattern are provided in discussion section 5.1.

SMF underestimated the SD in the early phenological stages but overestimated the SD in the late stages, which is opposite to the true pattern of change of SD with phenological stage (cf. the blue and black dashed lines in Fig. 10). It is interesting to observe that the relationship between the SMF-derived SD and phenological stages is almost a perfectly straight line; this seems to differ somewhat from the nonlinear quadric relationship derived from Eq. 5. To determine the reason for this linear result, we investigated the values of the two parameters *xscale* and *tshift*. We found that *tshift* had much smaller values (Fig. S4), suggesting that the last two terms in Eq. 5 are also very small and can be omitted (i.e., $D(p_{est}^i) = (p_0^i)^2 D(\frac{1}{xscale})$). The SMF-derived SD was thus reduced to:

$$SD(p_{est}^i) = \sqrt{D(p_{est}^i)} = p_0^i \sqrt{D\left(\frac{1}{xscale}\right)} \quad (12)$$

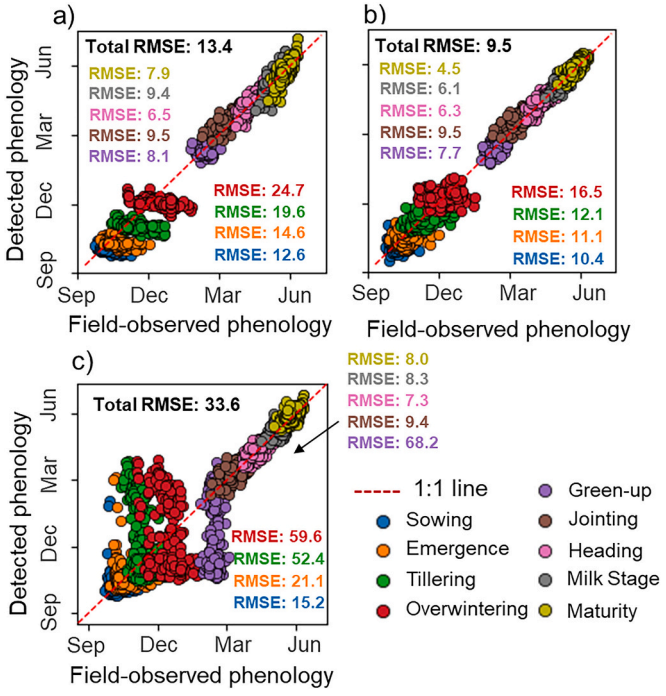

Fig. 9. Relationship between field-observed phenology and the phenology estimated by the (a) SMF, (b) SMF-S, and (c) SM-AGDD methods.

The above equation shows the approximately linear relationship between $SD(p_{est}^i)$ and p_0^i derived using SMF for ground-based phenology station experiments (Fig. 10). The small *tshift* values may be partially attributed to the difficulties experienced in SMF parameterization, which are discussed in depth in section 5.2.

We further investigated whether the SMF and SMF-S methods could capture temporal changes in crop phenology. Fig. 11 shows the correlation coefficients between the multiyear field phenology observations

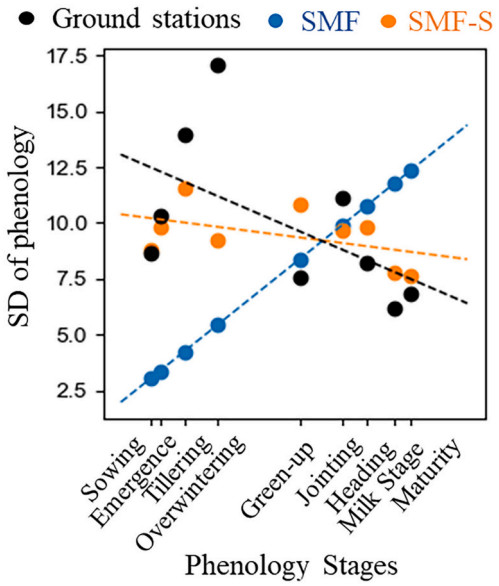

Fig. 10. Patterns of change in the phenology SD (standard deviation) versus the phenological stage. For the number of observations for each phenological stage, please refer to Table. 2.

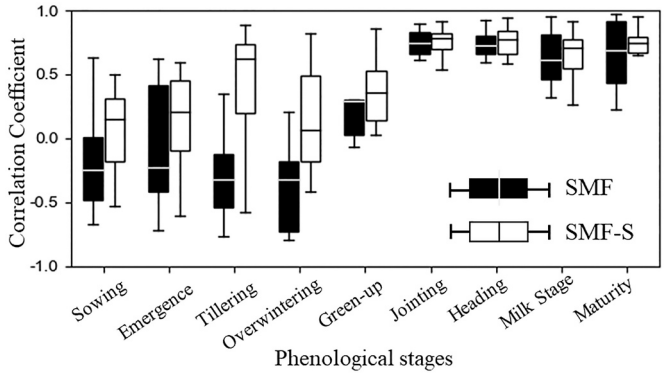

Fig. 11. Correlation coefficients between the multiyear field phenology observations and corresponding estimates for each phenological stage at each site. Each bar indicates the minimum, first quartile, median, third quartile, and maximum correlation coefficients.

and the corresponding estimates for each phenological stage. SMF-S achieved stronger correlations than SMF for all phenological stages, particularly in some early stages at which SMF even yielded negative correlations (Fig. 11). Such a pattern of negative correlations produced by SMF was due to unsynchronized changes in the length of the early and late phenological periods (see Fig. 14a; discussed in section 5.1).

4.3. Comparisons of winter wheat phenology mapping on the North China Plain

We compared the abilities of SMF-S and SMF to map winter wheat phenology on the North China Plain. The look-up table for the adaptive local windows in different winter wheat phenological stages is summarized in Table S1. Fig. 12 shows the estimations for emergence, spring green-up, and maturity date in 2008 as an example. The SMF-derived emergence varied between 285 and 295 DOY in the previous year, whereas the SMF-S-derived emergence varied more widely (Fig. 12a and 12b). At maturity, however, SMF yielded larger spatial variations. For example, SMF-derived maturity varied from as early as DOY 140 in the southwest area to DOY 170 in the northeast region (Fig. 12e). These

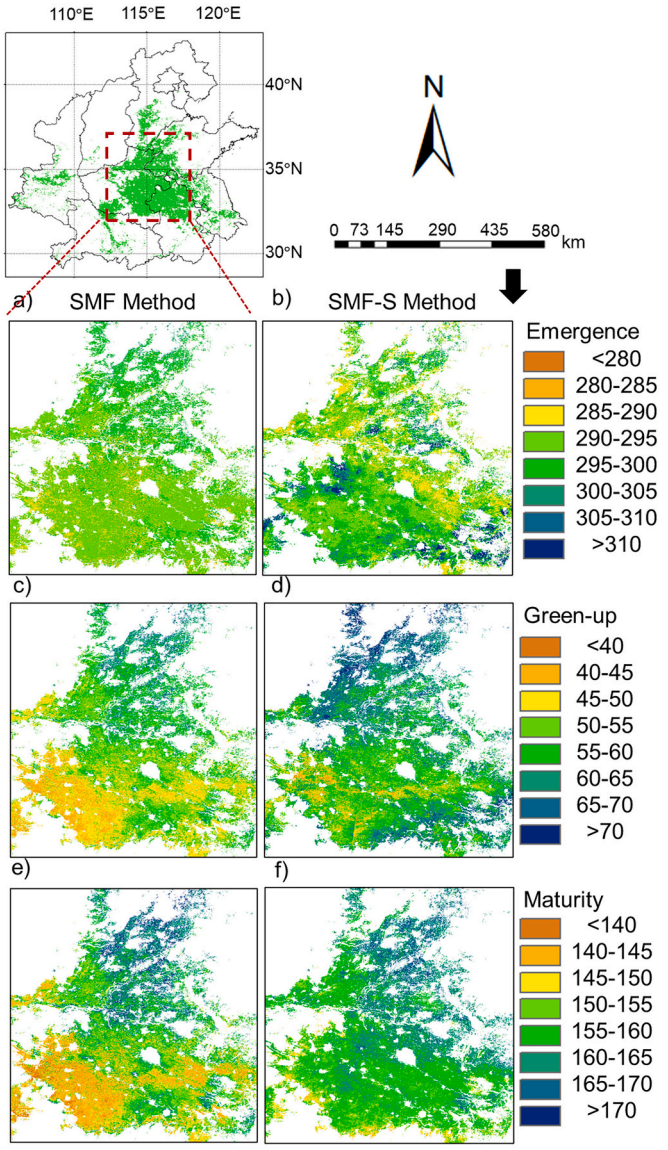

Fig. 12. Regional mapping results of (a, b) emergence (EMG), (c, d) the green-up date (GUD), and (e, f) the maturity (MD) date in 2008 obtained by the SMF and SMF-S methods.

spatial observations are consistent with the results from the ground stations, suggesting that the SMF underestimates (overestimates) the variations in early (late) phenological stages (Fig. 10). To further determine the reasons for their different performances, we drew histograms of phenology estimation differences between the two methods (i.e., SMF − SMF-S). In particular, we focused on the pixels distributed at the two ends of the histograms with large differences (i.e., the left 10% and right 10%; Fig. 13a). We averaged the EVI time series of these pixels and plotted the averaged phenological estimates on the curves. We assumed that the same phenological stages should be detected at approximately the same relative positions on the EVI time series. For those pixels at the two ends, the phenology estimates derived by SMF for the same phenological stage are not consistently distributed at the same positions on the curves (cf. Fig. 13b and 13c). For example, the SMF-derived maturity dates (Fig. 12e) are obviously earlier than the SMF-S-derived maturity dates in the southwest region (Fig. 12f), which is unrealistic owing to the obvious incorrect position on the EVI time-series curve (the blue point in Fig. 13b). In contrast, the phenological estimates provided by SMF-S exhibited more consistent relative positions on the EVI curves.

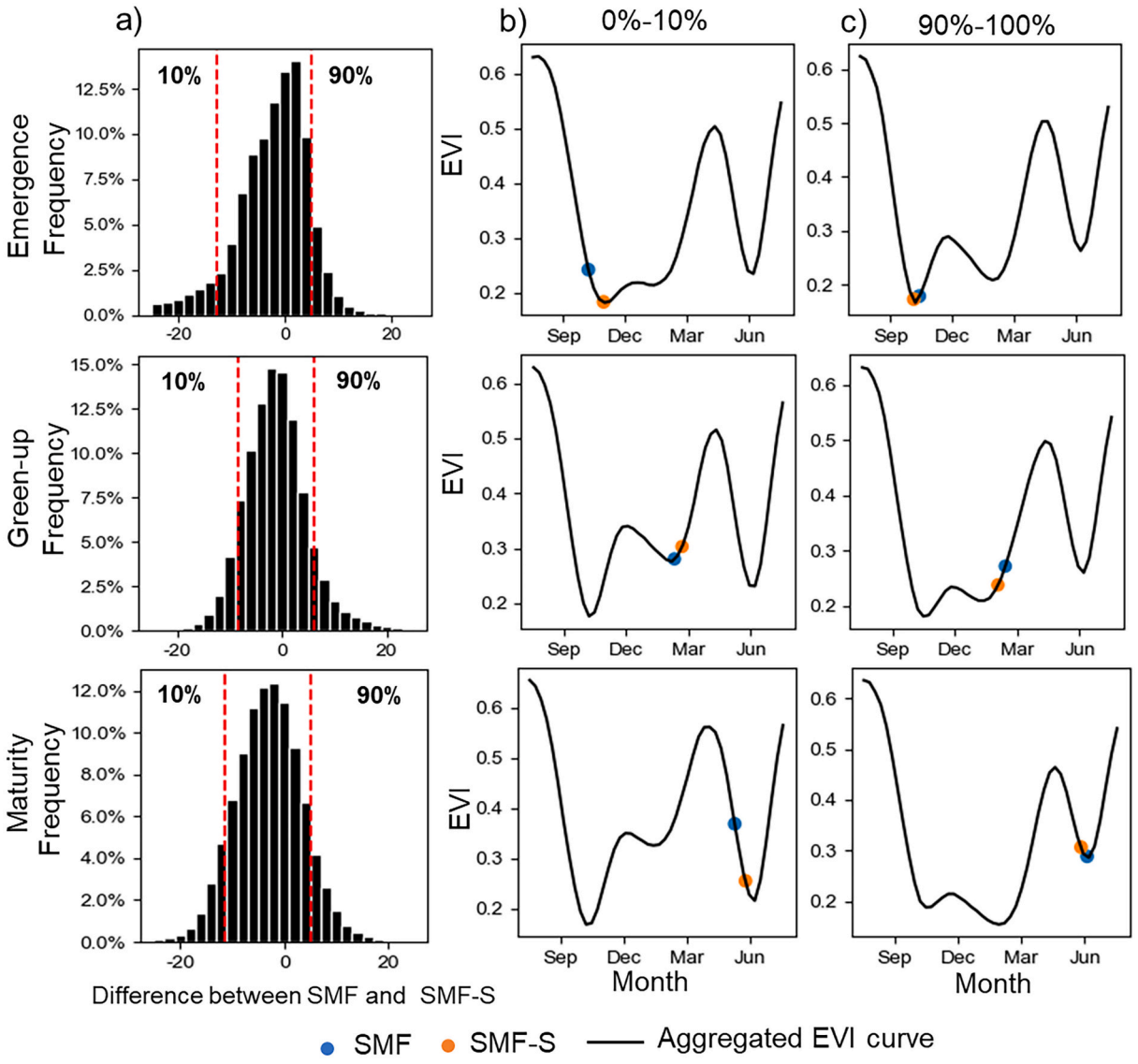

Fig. 13. (a) Histograms of the differences in phenology estimates between the SMF and SMF-S methods. The bin size of the histograms was set to 2 d. (b, c) Averaged EVI time series for the pixels at the two ends of the histograms. The colored points on the EVI curves reflect the averaged phenology estimates.

5. Discussion

5.1. Improvements in SMF-S

The challenge in monitoring crop phenology is how to accurately associate agronomic stages with satellite VI time series (Gao and Zhang, 2021). SMF is recognized as a promising method to address this challenge. In the SMF method, a reference curve containing the corresponding crop phenological stages (called a shape model) is matched with each target VI curve based on the assumption that the crop phenological stages are distributed at the same relative positions on the two curves (Sakamoto et al., 2010). The SMF-S method was developed from the SMF method and inherits the strengths of the shape model concept, such as its ability to combine ground-based agronomic observations with positions on curves of VI data. Moreover, the SMF-S method addresses two limitations of SMF.

First, SMF-S exhibits an improved ability to describe the relationships between multiple phenological stages. SMF adopts a global matching strategy with identical linear scaling and time shift factors; theoretically, the relationship between the lengths of any two phenological stages for the target pixels equals that in the shape model (see Eq. 3). To further illustrate this problem, we calculated the time intervals between the sowing and spring green-up stages and between the green-up and maturity stages by using winter wheat field phenology observations and corresponding phenology estimates derived using SMF and SMF-S. In actuality, the length of the early phenological period (i.e., green-up minus sowing) is significantly negatively correlated with the length of the late phenological period (i.e., maturity minus green-up) (Fig. 14a). Unfortunately, this negative correlation is incorrectly described as a positive proportional correlation when the phenological estimates are produced by SMF (Fig. 14b). In contrast, SMF-S can capture the negative correlation to some extent (Fig. 14c).

Unsynchronized changes in the lengths of the early and late phenological periods (Fig. 14a) contradict the positive proportional correlation estimated by SMF (Eq.3; Fig. 14 b). This suggests that it is impossible to match the shape model with all phenological stages well in this situation when using SMF. The objective of SMF is to minimize the RMSE between the geometrically transformed shape model and the NDVI time series. SMF tends to match the shape model with the late phenological stages of winter wheat because of the large NDVI values associated with these stages. Therefore, the early phenological stages may be poorly matched, and the matching performance in the late

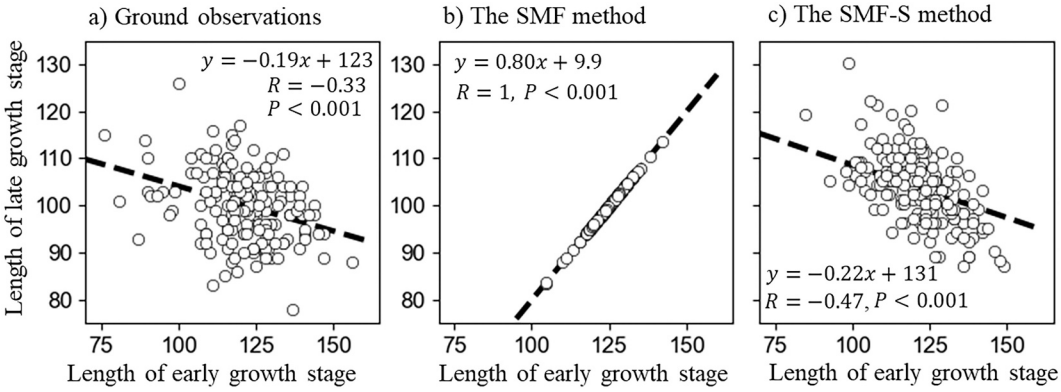

Fig. 14. Relationships between the time intervals of the early (the green-up date minus the sowing date) and late (the maturity date minus the green-up date) growth stages. All linear fits were significant (the ** symbol indicates significance at the $P < 0.01$ level).

phenological stages is more or less affected by the asynchronous changes in the two lengths (Fig. 14a). These relations may explain the poor performance of SMF in most phenological stages, particularly the early phenological stages, with negative correlations shown in Fig. 9a and Fig. 11. To further evaluate this explanation, a schematic diagram with a numerical example is given in Fig. S5. In actuality, asynchronous changes in different phenological stages are found in both natural vegetation (Jeong et al., 2011; Sun et al., 2020) and crops (Wang et al., 2021; Zhou et al., 2020). For example, changes in the length of the emergence period were opposite changes in the length of the tilling period for winter wheat between the two years considered (see Fig. Fig. 3 in Zhou et al., 2020). Thus, the improved ability of SMF-S to describe the relationships between phenological stages make it an excellent choice in many applications.

Second, SMF-S improves the ability to describe the spatial and temporal variations in each phenological stage. In SMF, the variance in the estimates of a particular phenological stage depends on the stage itself (Eq. 5). Our experimental results based on both field phenology observations and regional mapping confirm that SMF underestimates these spatial variations in the early phenological stages and overestimates the variations in late stages (Figs. 10 and 12). This result is due to the shape model used in SMF being stretched from the left endpoint. SMF-S addresses this problem by introducing the phenological stage into the shape model (Eq. 6); thus, stretching can be performed around both sides of each stage. Compared to those for natural vegetation, greater uncertainty may arise in the spatial and temporal variations in crop phenology because crop phenology is affected by both climate conditions and human activities (e.g., farmer practices and equipment availability) (He et al., 2015). The improved ability of SMF-S to simulate spatial and temporal variations in crop phenology could enhance the use of phenological information in crop growth management (Anderson et al., 2016).

SM-AGDD performed the worst in the winter wheat phenology estimation experiments (Fig. 9), with obviously larger estimation errors for the first five phenological stages. These results can be explained as follows. The early phenological stages are relatively concentrated in the VI-AGDD time series (Fig. 6B); thus, even a small matching error between the shape model and target curves can result in large phenology estimation errors for these stages. Generally, it is more difficult to achieve good matching performance in larger areas because climate conditions (e.g., temperature and precipitation) and crop varieties may differ substantially in space. Therefore, it is challenging to apply SM-AGDD with an identical shape model to the North China Plain area, which spans more than 1000 km (Fig. 4). One may wonder whether the performance can be improved when using SM-AGDD in local regions. To answer this question, we performed the winter wheat phenology detection experiment again but used a different shape model at each ground station. Specifically, the shape model at each ground station was generated by using the corresponding phenology observations in 2008 at the station. Winter wheat phenology from 2009–2016 at each station was thus detected using the shape model for the corresponding station. As we expected, the RMSE values averaged over all ground stations greatly decreased from 33.6 d to 17.0 d for SM-AGDD (Fig. S6). SMF-S still performed the best among the three methods in this additional experiment.

5.2. Parameter optimization in the SMF and SMF-S methods

Parameter optimization is an important step that may affect the performance of shape model fitting. For example, Zhou et al. (2020) suggested that the better performance of SM-AGDD than SM-APTT (Zeng et al., 2016) is partially due to the higher precision of scaling parameter optimization. SMF includes three parameters (*tshift*, *xscale*, and *yscale*) to be optimized. In our experiments, these parameters were originally optimized by using the nonlinear optimization procedure "L-BFGS-B" (Zhu et al., 1997) in the scipy-1.5.0 package of Python-3.8.3. To assess uncertainty in parameterization with SMF, one may adjust the parameter values and assess SMF performance when using different optimization procedures. To address this concern, we tested SMF by using the other four optimization procedures in the scipy-1.5.0 package. These procedures are called the "truncated Newton (TNC)" (Nash, 1984), "Powell" (Powell, 1964), "sequential least-squares programming (SLSQP)" (Kraft, 1988), and "Nelder–Mead" (Nelder and Mead, 1965) methods. In addition, we included the optimization procedure given by Sakamoto (2018) ("CONSTAINED_MIN" in the IDL program) in the tests. The results show that the RMSE values for SMF-derived phenology estimates obtained with all six optimization procedures are larger than the SMF-S RMSE values (cf. Fig. 9 and Fig. S7). We observed some differences in the parameter values when using different optimization procedures (Fig. S7). Two of the six optimization procedures ("TNC" and "Powell") yield larger *tshift* values, and the other four procedures generated similar parameter patterns with much smaller *tshift* values. We further checked the objective function of SMF and found that all six optimization procedures achieved similar minimum values (Fig. S8), suggesting that all the procedures can be considered effective for optimization. In SMF, the effect of *tshift* on the matching results can be offset to some extent by the effect of *xscale*. The six optimization procedures may utilize different rules to focus more on *tshift* or *xscale*, which may partially account for the different parameter values. Further mathematical demonstrations of the six nonlinear optimization procedures are beyond the scope of this study.

There are only two parameters to be optimized in the SMF-S shape model (i.e., $tshift_i$ and $xscale_i$). These parameters can be determined by traversing the parameter space with a simple iterative program (see the Methods section for details). Regarding the computational efficiency, our experiments show that SMF-S takes approximately half the time

required by SMF to detect a single phenological stage. However, SMF-S requires parameters to be optimized at each stage. In addition, more time is required when parameters must be traversed in larger parameter spaces, such as in cases with large differences between the shape model and target pixels.

5.3. Practical application of SMF-S

The first step in applying SMF-S is generating the shape model. There are three ways to do this according to the availability of phenology observations. The first is based on in situ phenology observations, in which the VI time series with corresponding phenological observations are directly extracted from field observation sites (Sakamoto et al., 2010). However, field observation sites may not be readily available in some applications. The second method is based on regional phenology reports (e.g., county-scale reports) (Sakamoto, 2018). First, the reference curve is generated by aggregating the regional VI time series for the same crop type. Then, the reference phenological stages are determined by minimizing the differences between the phenological estimates and regional-scale phenological reports. However, this method is characterized by low computational efficiency. The third method is based on the synthesis of multiyear VI time series; this method can be employed when phenological observations are unavailable. It generates the reference curve for each pixel by averaging the multiyear VI time series of the pixel and determines the reference phenology on the reference curve by applying phenology detection methods (e.g., the inflection method) (Chen et al., 2016). This method avoids the need to obtain field phenology observations and allows a unique shape model to be determined for each pixel. However, it is difficult to define crop phenological stages using this method without obvious inflection features. In practical applications, SMF-S can incorporate any of these three options to generate shape models depending on the availability of field-recorded phenology observations.

SMF-S uses an adaptive local window to reduce the influence of data noise on phenology detection. Our simulation experiments performed under the noise scenario confirmed the necessity of incorporating adaptive windows (Fig. 8). Because the range of noise levels in practical applications may not be as large as that in our simulation experiment, one may expect that a smaller-sized fixed window can be used for the objective of in-season phenology detection with SMF-S. Several recent studies have explored the detection of vegetation phenology within seasons (Gao et al., 2020; Gao and Zhang, 2021; Liu et al., 2018). Here, we estimated winter wheat phenology using fixed window sizes with w ranging from 30 to 120 d. Comparing the results with field phenology observations showed that the phenology estimates using any fixed window were worse than the estimates derived using adaptive local windows (Fig. 15). To detect crop phenology within a season based on SMF-S, a fixed window with a smaller size (e.g., w =30 d) may be used but will result in a certain decrease in the detection accuracy. In addition, the application of SMF-S within seasons has two requirements. First, crop type information is required when detecting crop phenology using SMF-S. Identifying crop types before the growing season may be possible only in agricultural areas with regular crop rotations, as the current-year crop types in these areas can be predicted from historical crop planting maps (Zhang et al., 2019). Recently, some studies have also conducted in-season crop classifications (e.g., Johnson and Mueller, 2021). The impacts of in-season crop identification on in-season crop phenology detection are worth investigating in the future. Second, high-quality NDVI data are required for phenology detection based on limited NDVI time series within a season (Zhang et al., 2012). However, the quality of MODIS NDVI data may be unsatisfactory in some cloudy areas, where larger local windows are required in SMF-S to achieve reliable phenology estimates, thus decreasing the timeliness of phenology detection. For areas with heterogeneous croplands, NDVI series with high spatial resolutions (e.g., Sentinel-2) are necessary, but serious data gaps may exist in these series (Chen et al., 2021). One promising technique to solve this issue is the fusion of optical and synthetic aperture radar (SAR) time series, which has proven effective for dynamic crop monitoring (Zhao et al., 2020a).

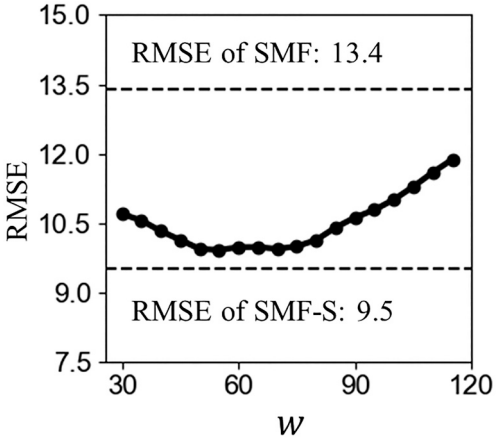

Fig. 15. Accuracy of winter wheat phenology estimates obtained with SMF-S using different fixed local window sizes. The two dashed lines indicate the RMSE value for SMF-S with adaptive local windows and SMF.

We tested the superiority of SMF-S to other methods in detecting winter wheat phenology on the North China Plain. Winter wheat has a long growing season with two growth peaks (Dong et al., 2020; Qiu et al., 2017). Multiple phenological stages in the growing season correspond to important tasks. For example, the tillering date and jointing stage affect irrigation management (Zhao et al., 2020b), and the sowing and harvest dates help yield estimations (Sun et al., 2007). Theoretically, SMF-S can be applied to other crop types (e.g., maize or soybean). The errors in the maize and soybean phenology estimates obtained by SMF were reported to be smaller than 5 d (Sakamoto, 2018; Zeng et al., 2016); these results may have been associated with the relatively short growing seasons of these crops. However, inherent limitations still exist in such estimates derived by SMF, such as the dependence of the phenological variance on the phenological stage.

6. Conclusion

Regional-scale crop phenology can be determined using satellite remote sensing data. In this study, we proposed the SMF-S method to estimate crop phenology from VI time series. The proposed method improves upon the SMF method, which has difficulty describing the relationships among multiple phenological stages and simulating the spatial variances in individual stages. The SMF-S method, in contrast, modifies the fitting function and adopts an iterative procedure to match the shape model with the VI time series for each stage in an adaptive local window. We tested the effectiveness of SMF-S using multisource data. SMF-S performed better than SMF, producing lower estimation errors under the no-noise scenario in the simulation experiments (average RMSE: 0.72 vs. 5.19 d). In the scenario in which different noise levels were considered, the SMF-S performance was also better than the SMF performance, thanks to the use of adaptive local windows. We further evaluated the SMF-S method by detecting the winter wheat phenology on the North China Plain. The SMF-S estimates were more consistent with the field phenology observations than were the results of SMF and SM-AGDD (average RMSEs: 9.5, 13.4 d and 33.6 d, respectively). SMF-S also better described the spatial variations (i.e., variance) and captured the temporal shifts in multiple phenological stages. By analyzing the generated regional winter wheat phenology maps, we found that SMF underestimated the spatial variations in the early phenological stages and overestimated those in late stages. SMF-S addressed this problem and generated more reasonable regional phenology mapping results. The SMF-S code is available from the link:

https://github.com/LicongLiu/SMF_S_Release.

CRediT authorship contribution statement

Licong Liu: Data curation, Methodology, Software, Writing – original draft. **Ruyin Cao:** Conceptualization, Methodology, Writing – original draft, Supervision. **Jin Chen:** Conceptualization, Writing – review & editing. **Miaogen Shen:** Writing – review & editing. **Shuai Wang:** Writing – review & editing. **Ji Zhou:** Writing – review & editing. **Binbin He:** Writing – review & editing.

Declaration of Competing Interest

The authors declare that they have no known competing financial interests or personal relationships that could have appeared to influence the work reported in this paper.

Acknowledgments

This work was funded by the 2nd Scientific Expedition to the Qinghai-Tibet Plateau (2019QZKK0307) and the Sichuan Science and Technology Program (2022YFH0106 and 2021YFG0028).

Appendix A. Appendix

Here, we provide the corrigendum to the phenology estimation equation used in the SMF method considering the mistakes made in previous studies (Sakamoto et al., 2010; Sakamoto, 2018).

(1) The mistake and its correction

In SMF, the geometrical fitting of the shape model on the target curves (i.e., Eq. 3 in Sakamoto, 2018) is expressed as follows:

$$h(\mathrm{x}) = \mathrm{yscale} \times [g(xscale \times (x + tshift)) + bias] - bias \tag{A1}$$

where $g(x)$ represents the shape model and $h(x)$ is the geometrically transformed shape model. After acquiring the two required parameters (i.e., *xscale* and *tshift*) through optimization, Sakamoto (2018) estimated the phenology of the target curve (X_{est}) by substituting the defined phenology (X_0) into the following equation:

$$X_{est} = xscale \times (X_0 + tshift) \tag{A2}$$

However, **Eq. (A2) is incorrect.** This may be due to confusion regarding the difference between the scaling and shifting of the function (i.e., $g(x)$) and a point (X_0). For example, if *tshift* is positive and *xscale* is larger than 1.0, "$g(xscale \times (x + tshift))$" in Eq. (A1) would suggest that $g(x)$ is first moved left by *tshift* and then shrunken due to *xscale*. This operation is, however, opposite the "$xscale \times (X_0 + tshift)$" expression in Eq. (A2), in which the X_0 point in $g(x)$ is first moved right by *tshift* and is then stretched by *xscale*. Because neither yscale nor *bias* in Eq. A1 affect the x (date) dimension, we assume they are 1.0 and 0.0, respectively. Thus, Eq. (A1) can be reduced to the following expression:

$$h(\mathrm{x}) = g(xscale \times (x + tshift)) \tag{A3}$$

X_{est} in $h(\mathrm{x})$ is estimated from X_0 in $g(x)$ by scaling and shifting. However, it should be noted that the *xscale* and *tshift* values determined in Eq. (A3) are the scaling and shifting factors for the $g(x)$ function. Point X_0 can be formulated as follows:

$$xscale \times (X_{est} + tshift) = X_0 \tag{A4}$$

Therefore, Eq. (A2) should be corrected as follows:

$$X_{est} = \frac{1}{xscale} X_0 - tshift \tag{A5}$$

(2) A numerical test of Eq. (A5)

For a shape model "$g(x) = 0.5x - 1$" (represented by the orange line in Fig. A1), the geometrically transformed shape model is formulated as follows: "$h(\mathrm{x}) = g(2 \times (x + 1)) = x$" (i.e., *tshift*=1 and *xscale*=2; see the blue dashed line in Fig. A1). Assuming that X_0=6, X_{est} is estimated to be 14 according to Eq. (A2), but this value is obviously incorrect. Based on Eq. (A6), we can achieve the correct X_{est} value of 2.

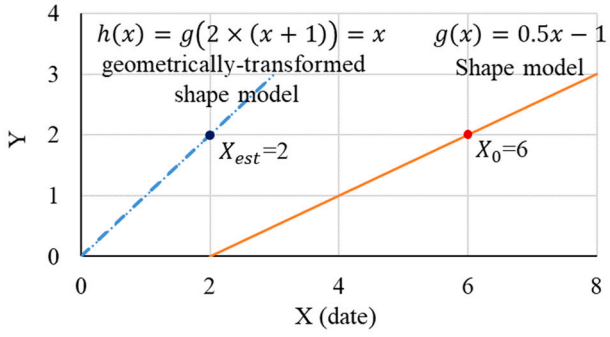

Fig. A1. Numerical test results for the shape model (orange line) and the geometrically transformed shape model (blue dashed line).

Appendix B. Supplementary data

Supplementary data to this article can be found online at https://doi.org/10.1016/j.rse.2022.113060.

References

Anderson, M.C., Hain, C.R., Jurecka, F., Trnka, M., Hlavinka, P., Dulaney, W., Otkin, J. A., Johnson, D., Feng, G., 2016. Relationships between the evaporative stress index and winter wheat and spring barley yield anomalies in the Czech Republic. Clim. Res. 70, 215–230.

Beck, P.S., Atzberger, C., Høgda, K.A., Johansen, B., Skidmore, A.K., 2006. Improved monitoring of vegetation dynamics at very high latitudes: a new method using MODIS NDVI. Remote Sens. Environ. 100, 321–334.

Bhogapurapu, N., Dey, S., Bhattacharya, A., Mandal, D., Lopez-Sanchez, J.M., McNairn, H., López-Martínez, C., Rao, Y.S., 2021. Dual-polarimetric descriptors from Sentinel-1 GRD SAR data for crop growth assessment. ISPRS J. Photogramm. Remote Sens. 178, 20–35.

Bolton, D.K., Friedl, M.A., 2013. Forecasting crop yield using remotely sensed vegetation indices and crop phenology metrics. Agric. For. Meteorol. 173, 74–84.

Boschetti, M., Stroppiana, D., Brivio, P.A., Bocchi, S., 2009. Multi-year monitoring of rice crop phenology through time series analysis of MODIS images. Int. J. Remote Sens. 30, 4643–4662.

Brown, M., De Beurs, K., Marshall, M., 2012. Global phenological response to climate change in crop areas using satellite remote sensing of vegetation, humidity and temperature over 26 years. Remote Sens. Environ. 126, 174–183.

Cao, R., Chen, J., Shen, M., Tang, Y., 2015. An improved logistic method for detecting spring vegetation phenology in grasslands from MODIS EVI time-series data. Agric. For. Meteorol. 200, 9–20.

Cao, R., Chen, Y., Shen, M., Chen, J., Zhou, J., Wang, C., Yang, W., 2018a. A simple method to improve the quality of NDVI time-series data by integrating spatiotemporal information with the Savitzky-Golay filter. Remote Sens. Environ. 217, 244–257.

Cao, R., Shen, M., Zhou, J., Chen, J., 2018b. Modeling vegetation green-up dates across the Tibetan Plateau by including both seasonal and daily temperature and precipitation. Agric. For. Meteorol. 249, 176–186.

Chen, J., Jönsson, P., Tamura, M., et al., 2004. A simple method for reconstructing a high-quality NDVI time-series data set based on the Savitzky-Golay filter. Remote Sens. Environ. 91, 332–344.

Chen, J., Rao, Y., Shen, M., Wang, C., Zhou, Y., Ma, L., Tang, Y., Yang, X., 2016. A simple method for detecting phenological change from time series of vegetation index. IEEE Trans. Geosci. Remote Sens. 54, 3436–3449.

Chen, Y., Cao, R., Chen, J., et al., 2021. A practical approach to reconstruct high-quality Landsat NDVI time-series data by gap filling the Savitzky-Golay filter. ISPRS J. Photogramm. Remote Sens. 180, 174–190.

Diao, C., 2019. Innovative pheno-network model in estimating crop phenological stages with satellite time series. ISPRS J. Photogramm. Remote Sens. 153, 96–109.

Dong, Q., Chen, X., Chen, J., Zhang, C., Cui, X., 2020. Mapping winter wheat in north China using Sentinel 2A/B data: a method based on phenology-time weighted dynamic time warping. Remote Sens. 12, 1274.

Gao, F., Zhang, X., 2021. Mapping crop phenology in near real-time using satellite remote sensing: Challenges and opportunities. J. Remote Sens. 2021, 8379391.

Gao, F., Anderson, M., Daughtry, C., Karnieli, A., Hively, D., Kustas, W., 2020. A within-season approach for detecting early growth stages in corn and soybean using high temporal and spatial resolution imagery. Remote Sens. Environ. 242, 111752.

Guo, L., An, N., Wang, K., 2016. Reconciling the discrepancy in ground- and satellite-observed trends in the spring phenology of winter wheat in China from 1993 to 2008. J. Geophys. Res.-Atmos. 121, 1027–1042.

He, L., Asseng, S., Zhao, G., Wu, D., Yang, X., Zhuang, W., Jin, N., Yu, Q., 2015. Impacts of recent climate warming, cultivar changes, and crop management on winter wheat phenology across the Loess Plateau of China. Agric. For. Meteorol. 200, 135–143.

Jeong, S.-J., Ho, C.-H., Gim, H.-J., Brown, M.E., 2011. Phenology shifts at start vs. end of growing season in temperate vegetation over the Northern Hemisphere for the period 1982–2008. Glob. Chang. Biol. 17, 2385–2399.

Johnson, D.M., Mueller, R., 2021. Pre- and within-season crop type classifcation trained with archival land cover information. Remote Sens. Environ. 264, 112576.

Kraft, D., 1988. A software package for sequential quadratic programming. Tech. Rep. DFVLR-FB 88–28. DLR German Aerospace Center – Institute for Flight Mechanics, Koln, Germany.

Liu, L., Zhang, X., Yu, Y., Gao, F., Yang, Z., 2018. Real-time monitoring of crop phenology in the midwestern United states Using VIIRS observations. Remote Sens. 10, 1540.

Manfron, G., Delmotte, S., Busetto, L., Hossard, L., Ranghetti, L., Brivio, P.A., Boschetti, M., 2017. Estimating inter-annual variability in winter wheat sowing dates from satellite time series in Camargue, France. Int. J. Appl. Earth Obs. Geoinf. 57, 190–201.

Nash, S.G., 1984. Newton-Type Minimization Via the Lanczos Method. SIAM J. Num. Analysis 21, 770–778.

Nelder, J.A., Mead, R., 1965. A Simplex Method for Function Minimization. Comput. J. 7, 308–313.

Powell, M.J.D., 1964. An efficient method for finding the minimum of a function of several variables without calculating derivatives. Comput. J. 7, 155–162.

Qiu, B., Luo, Y., Tang, Z., Chen, C., Lu, D., Huang, H., Chen, Y., Chen, N., Xu, W., 2017. Winter wheat mapping combining variations before and after estimated heading dates. ISPRS J. Photogramm. Remote Sens. 123, 35–46.

Sakamoto, T., 2018. Refined shape model fitting methods for detecting various types of phenological information on major U.S. crops. ISPRS J. Photogramm. Remote Sens. 138, 176–192.

Sakamoto, T., Yokozawa, M., Toritani, H., Shibayama, M., Ishitsuka, N., Ohno, H., 2005. A crop phenology detection method using time-series MODIS data. Remote Sens. Environ. 96, 366–374.

Sakamoto, T., Wardlow, B.D., Gitelson, A.A., Verma, S.B., Suyker, A.E., Arkebauer, T.J., 2010. A Two-Step Filtering approach for detecting maize and soybean phenology with time-series MODIS data. Remote Sens. Environ. 114, 2146–2159.

Schlund, M., Erasmi, S., 2020. Sentinel-1 time series data for monitoring the phenology of winter wheat. Remote Sens. Environ. 246, 111814.

Shang, R., Liu, R.G., Xu, M.Z., Liu, Y., Zuo, L., Ge, Q.S., 2017. The relationship between threshold-based and inflexion-based approaches for extraction of land surface phenology. Remote Sens. Environ. 199, 167–170.

Sun, H., Zhang, X., Chen, S., Pei, D., Liu, C., 2007. Effects of harvest and sowing time on the performance of the rotation of winter wheat–summer maize in the North China Plain. Ind. Crop. Prod. 25, 239–247.

Sun, Q., Li, B., Zhou, G., Jiang, Y., Yuan, Y., 2020. Delayed autumn leaf senescence date prolongs the growing season length of herbaceous plants on the Qinghai–Tibetan Plateau. Agric. For. Meteorol. 284, 107896.

Sun, L., Gao, F., Xie, D., Anderson, M., Chen, R., Yang, Y., Yang, Y., Chen, Z., 2021. Reconstructing daily 30 m NDVI over complex agricultural landscapes using a crop reference curve approach. Remote Sens. Environ. 253, 112156.

Wang, S., Chen, J., Rao, Y., Liu, L., Wang, W., Dong, Q., 2020. Response of winter wheat to spring frost from a remote sensing perspective: damage estimation and influential factors. ISPRS J. Photogramm. Remote Sens. 168, 221–235.

Wang, W., Zhang, X., Shang, Z., 2021. Variation characteristics in growth stages of winter wheat (Triticum Aestivum L.) and prediction model. *Bangladesh*. J. Botany 50 (3), 737–746.

Wardlow, B.D., Kastens, J.H., Egbert, S.L., 2006. Using USDA crop progress data for the evaluation of greenup onset date calculated from MODIS 250-meter data. Photogramm. Eng. Remote Sens. 72, 1225–1234.

Yang, Y., Ren, W., Tao, B., Ji, L., Liang, L., Ruane, A.C., Fisher, J.B., Liu, J., Sama, M., Li, Z., Tian, Q., 2020. Characterizing spatiotemporal patterns of crop phenology across North America during 2000–2016 using satellite imagery and agricultural survey data. ISPRS J. Photogramm. Remote Sens. 170, 156–173.

Yang, Y., Tao, B., Liang, L., Huang, Y., Ren, W., 2021. Detecting recent crop phenology dynamics in corn and soybean cropping systems of Kentucky. Remote Sens. 13, 1615.

Zeng, L., Wardlow, B.D., Wang, R., Shan, J., Tadesse, T., Hayes, M.J., Li, D., 2016. A hybrid approach for detecting corn and soybean phenology with time-series MODIS data. Remote Sens. Environ. 181, 237–250.

Zeng, L., Wardlow, B.D., Xiang, D., Hu, S., Li, D., 2020. A review of vegetation phenological metrics extraction using time-series, multispectral satellite data. Remote Sens. Environ. 237, 111511.

Zhang, X., Friedl, M.A., Schaaf, C.B., Strahler, A.H., Hodges, J.C.F., Gao, F., Reed, B.C., Huete, A., 2003. Monitoring vegetation phenology using MODIS. Remote Sens. Environ. 84, 471–475.

Zhang, C., Di, L.P., Lin, L., Guo, L.Y., 2019. Machine-learned prediction of annual crop planting in the U.S. Corn Belt based on historical crop planting maps. Comput. Electron. Agric. 166, 104989.

Zhang, X, Goldberg, M, Yu, Y, 2012. Prototype for monitoring and forecasting fall foliage coloration in real time from satellite data. Agri. For. Meteorol. 158, 21–29.

Zhang, X., Wang, J., Henebry, G.M., Gao, F., 2020. Development and evaluation of a new algorithm for detecting 30 m land surface phenology from VIIRS and HLS time series. ISPRS J. Photogramm. Remote Sens. 161, 37–51.

Zhao, J., Han, T., Wang, C., Jia, H., Worqlul, A.W., Norelli, N., Zeng, Z., Chu, Q., 2020a. Optimizing irrigation strategies to synchronously improve the yield and water productivity of winter wheat under interannual precipitation variability in the North China Plain. Agric. Water Manag. 240, 106298.

Zhao, W., Qu, Y., Chen, J., et al., 2020b. Deeply synergistic optical and SAR time series for crop dynamic monitoring. Remote Sens. Environ. 247, 111952.

Zhong, L., Hu, L., Yu, L., Gong, P., Biging, G.S., 2016. Automated mapping of soybean and corn using phenology. ISPRS J. Photogramm. Remote Sens. 119, 151–164.

Zhou, M., Ma, X., Wang, K., Cheng, T., Tian, Y., Wang, J., Zhu, Y., Hu, Y., Niu, Q., Gui, L., Yue, C., Yao, X., 2020. Detection of phenology using an improved shape model on time-series vegetation index in wheat. Comput. Electron. Agric. 173, 105398.

Zhu, C., Byrd, R.H., Lu, P., Nocedal, J., 1997. Algorithm 778: L-BFGS-B: Fortran subroutines for large-scale bound-constrained optimization. ACM Trans. Math. Softw. 23, 550–560.